Onset of High-Harmonic Fast Wave Propagation in Annulus Geometry

Seung-Gyou Baek[1*], *Ricardo* De Levante Rodriguez[1], *Nicola* Bertelli[2], *Paul* Bonoli[1], and *Syun'ichi* Shiraiwa[2]

[1]MIT Plasma Science and Fusion Center, 02139 Cambridge, MA, USA
[2]Princeton Plasma Physics Laboratory, 08540 Princeton, NJ, USA

Abstract. Previous experiments on NSTX have reported high-harmonic fast wave (HHFW) power losses in the scrape-off layer (SOL), with dependencies on the wave parallel wavenumber, plasma density, and magnetic field. This study presents an analysis of HHFW propagation in the SOL plasma, focusing on parasitic coupling to the waveguide mode bounded by the steep gradient pedestal and the outer wall boundary. The analytic and finite element wave models are discussed using a 2D annulus geometry, which serves as a simplified representation of the NSTX-U plasma. The model shows that a minimum radial gap width is required to support wave propagation, analogous to the higher-order modes in coaxial geometries. The impact of several factors, including gap width, wave parallel phasing, and magnetic field strength, on parasitic wave coupling is examined, highlighting the role of the geometric dimension in relation to the wave perpendicular wavelength. The findings suggest that controlling the edge/SOL density profile (gap control) is crucial for mitigating parasitic coupling when the density in front of the antenna exceeds the density cutoff.

1 Introduction

This paper discusses a waveguide mode in the 2D annulus geometry of an anisotropic plasma medium, aiming to provide a mechanism for the onset of propagating high-harmonic fast waves (HHFWs) in scrape-off-layer (SOL) plasmas, as observed in past experiments and numerical simulations of HHFWs on the NSTX-U spherical tokamak.

In past NSTX experiments, up to 60% of the HHFW power launched from the 12-strap antenna was found to be lost in the SOL on the first pass [1]. Specifically, the loss exhibited a clear dependence on the wave parallel wavenumber $k_\parallel$ (as imposed by the antenna), plasma density, and magnetic field. Heating efficiency is significantly improved at a higher $k_\parallel$, higher B-field, and at lower edge and SOL densities. Such a dependence pointed to the role of the onset of fast wave propagation in the SOL above the right-hand (R) density cut-off ($n_\parallel^2 = R = 1 - \sum_j \omega_{pj}^2/(\omega(\omega + \Omega_{cj}))$, where $n_\parallel = ck_\parallel/\omega$ is the wave parallel refractive index, ω is the wave frequency, and ω_{pj} is the plasma frequency of the species with the index j, and Ω_{cj} is the cyclotron frequency [2]. Note that the R-cutoff density is approximately a function of $n_{cut} \propto k_\parallel^2 B/\omega$.

Subsequent simulation efforts using full-wave codes, such as AORSA [3,4], FW2D [5], and Petra-M [6], have successfully identified the appearance of a wavefield restricted to the edge/SOL plasma region between the vacuum vessel and the steep pedestal, termed as the surface wave or cavity mode. One of the salient features in the modelling is that the onset of the propagating wavefield structure in the SOL correlates with an increased level of collisional damping, a proxy for edge losses, following the experimental parametric dependence on key parameters such as phasing, density, and field. Based on the experiments and simulations, the onset of HHFW propagation into the SOL (or the loss of heating efficiency) has been correlated with the opening of the fast wave cut-off layer in front of the antenna. The results suggest that low-density operation in front of the HHFW antenna enhances core coupling, unlike the low-harmonic ion cyclotron range of frequencies (ICRF) heating scenario, where high edge/SOL density is desired for maximal loading resistance. Therefore, bridging our understanding of coupling physics between the HHFW and ICRF regimes remains.

This paper discusses a higher-order annulus (or coaxial) waveguide mode [7] as a propagation mechanism of the HHFW wave that is restricted to the SOL region. The wave propagation in the annulus SOL region can still be guided between the conducting vacuum vessel and the steep pedestal, which acts as a reflection layer with a greater impedance mismatch. For its propagation, the minimum radial (transverse) width condition remains the same as annulus resonance [8], i.e., the half-wavelength standing wave needs to be formed in the radial direction for wave propagation in the axial (toroidal) direction. It will be discussed that the geometric requirement is unlikely to be met in a typical ICRF regime due to a relatively long wavelength. This mode is analogous to the higher-order mode in the coaxial geometry, which is supported above the cutoff frequency, in addition to the fundamental transverse electromagnetic (TEM) mode. In a plasma medium,

* Corresponding author: sgbaek@psfc.mit.edu

however, the anisotropic medium is filled, and the density above the R-cutoff is a prerequisite for this mode.

While annulus resonance is thought to be an excitation mechanism for this waveguide mode, this discussion will not be within the scope of this work. Annulus resonance has been proposed as a fast wave power coupling (or, to be precise, field enhancement) mechanism to the SOL plasma. The wave matching conditions across the interface regions (e.g., core-SOL-vacuum in that 2D cylinder model) predict a wave structure whose radial dimension is *also* a standing wave in the annulus SOL when its radial width equals one-half of the perpendicular wavelength. This formalism assumes the establishment of the cavity field in both the plasma core and the annular SOL regions without considering the absorption or dissipation of the wave power. Therefore, its possible connection to the waveguide mode discussed here will be reported in future work.

The organization of this paper is as follows. Section 2 introduces the past full-wave HHFW modelling of the density scan, showing that the occurrence of fast wave propagation in the SOL coincides with the gap width being greater than half the perpendicular wavelength. Section 3 discusses the analytic model in the 2D coaxial geometry. Section 4 presents the Petra-M full-wave simulation using a 2D geometry to illustrate the parametric dependencies of the mode onset on wave phasing, density, field, and gap width. Section 5 is a discussion and summary.

2 Onset of fast wave propagation vs. SOL gap width

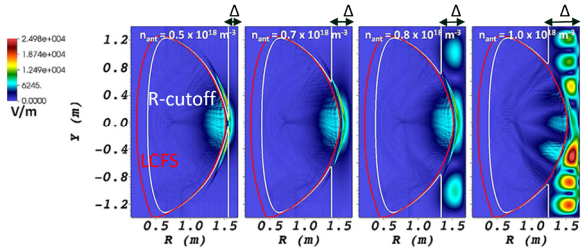

Fig. 1. Dependence of fast wave propagation in the SOL on the minimum density. The wave electric field is shown at four different minimum antenna densities: n_{ant} = 0.5, 0.7, 0.8, and 1.0×10^{18} m^{-3}. $k_{||}$ = 6.6 m^{-1}, f_0 = 30 MHz, B_0 = 0.51 T, and B_{SOL} = 0.28 T. Figure is adapted from Figure 13 in [9], reproduced with permission from the IAEA Nuclear Fusion journal.

As shown in Fig. 1, past HHFW modelling reproduces the experimental trend of HHFW power coupling to the SOL as a function of density. The opening of the R cut-off layer in front of the antenna (denoted by the white curve in the figure) at the low field side is correlated with the onset of HHFW propagation into the SOL, which is bounded by the R cut-off and the outer simulation domain (perfect electric conductor boundary condition). Nevertheless, the opening of the cut-off layer does not automatically lead to fast wave propagation, as shown in the second case (the minimum density of n_{ant} = $0.7\text{x}10^{18}$ m^{-3}), suggesting an intermediate SOL density range exists without SOL propagation.

Therefore, it is thought that an additional constraint exists, which is related to the geometry. A higher-order transverse electric (TE) mode is hypothesized to be guided by the SOL plasma for the HHFW regime due to its shorter and comparable wavelength to the SOL gap width. Table 1 compares the wave perpendicular half wavelength ($\Delta_{crit} = \lambda_\perp/2$) with the horizontal gap width (Δ) between the R-cutoff and the wall in the simulation domain, as marked in Fig. 1. The half-perpendicular wavelength is shorter than the gap width in the simulation domain only in the last two high density cases (n_{ant} = 0.8 and 1.0×10^{18} m^{-3}), and a standing wave field pattern is expected to be supported by the geometry, coinciding with the simulation results. This view also supports previous simulation results that low harmonic ICRF does not exhibit parasitic coupling to the SOL, even with the complete opening of the R-cutoff in front of the antenna [9], due to its much longer perpendicular wavelength. For example, on Alcator C-Mod, the 80 MHz ICRF wave at 4 T possesses the half perpendicular wavelength of $\lambda_\perp/2$ = 55 cm for k_φ=7.5 m^{-1} at the SOL density of 8.0×10^{18} m^{-3}, which is much longer than a plasma SOL width of ~3 cm.

Table 1. Comparison of the annulus gap width (Δ) in Fig.1 with the wave perpendicular wavelength at four SOL densities.

n_{ant} (10^{18} m^{-3})	Gap Width Δ (cm)	$\lambda_\perp/2$ (cm)
0.5	~14	63
0.7	~30	32
0.8	~36	36
1.0	~46	21

3 TE mode in the coaxial (annular) configuration

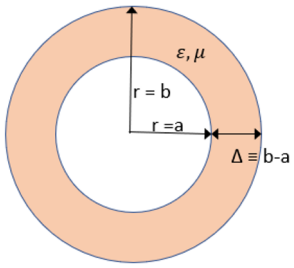

Fig. 2. Coaxial plasma geometry with the inner radius of *a* and the outer radius of *b* with the perfect electric boundary conditions. The annulus region is filled with a plasma medium (permittivity of ε and permeability of μ). The annulus gap width is $\Delta \equiv b - a$.

Fig. 2 shows a simplified 2D coaxial (annular) cylinder geometry. In the coaxial configuration, higher-order modes can be excited with a cut-off wavenumber (or frequency) condition, in addition to the fundamental

TEM mode. This condition is similar to the parallel plate waveguide mode, where a standing wave in the transverse direction is required with the cutoff wavenumber condition: $k_c = \frac{l\pi}{\Delta}$, where Δ is the width between the two plates and l is the harmonic number l = 1, 2, 3… The propagation wavenumber of the TE_l mode is given by $k_z = \sqrt{k^2 - \left(\frac{l\pi}{d}\right)^2} > 0$, and the total wavenumber needs to be greater than the minimum radial wavenumber condition. For the azimuthal mode number (n = 1) TE_{11} case [8], the corresponding cutoff wavenumber and frequency are $k_c = \frac{2}{a+b}$ and $f_c = \frac{ck_c}{2\pi\sqrt{\varepsilon_r}} = \frac{c}{\pi(a+b)\sqrt{\varepsilon_r}}$, respectively.

A similar situation can be anticipated in the HHFW experiment/modeling between the vacuum vessel wall and the steep pedestal. Given the HHFW nature whose electric field is normal to the background magnetic field, the transverse electric (TE) mode is considered. The boundary condition is that the parallel component of the wave electric field component is zero assuming a perfect electric conductor condition at the two boundaries: E_θ (a) = E_θ (b) = 0. The plasma is represented by a dielectric tensor $\bar{\bar{\epsilon}}$:

$$\bar{\bar{\epsilon}} = \begin{pmatrix} S & -iD & 0 \\ iD & S & 0 \\ 0 & 0 & P \end{pmatrix},$$

where S, D, and P are the cold plasma tensor elements in the Stix form [2]. The wavefield is assumed to propagate in the axial direction (z-direction) with the Fourier mode: $\boldsymbol{E} = \boldsymbol{E}(\mathrm{r})e^{i(k_z z + m\theta - \omega t)}$. From the Maxwell's equations, the wave equation for the B_z component can be written :

$$\nabla_\perp^2 B_z - \frac{(\mathrm{k}_z^2 - \epsilon_{xx})^2 + \epsilon_{xy}^2}{\mathrm{k}_z^2 - \epsilon_{xx}} B_z = 0,$$

where $\epsilon_{xx} = (\omega^2/c^2)S$, $\epsilon_{xy} = -\mathrm{i}\,(\omega^2/c^2)D$, and $\nabla_\perp^2 = \frac{1}{r}\frac{\partial}{\partial r}\left(r\frac{\partial}{\partial x}\right) + \frac{1}{r^2}\frac{\partial}{\partial \theta^2}$ is the Laplacian operator for the perpendicular component. Note that, in the MHD limit ($\omega \ll \omega_{ci}$), $\epsilon_{xx} \approx c^2/v_A^2$ and $\epsilon_{xy} \propto \frac{\omega}{\omega_{ci}}\epsilon_{xx} \approx 0$, where $v_A = B/\sqrt{\mu_0 m_i n_i}$ is the Alfven speed. The dispersion relation becomes that of the compressional Alfven wave:

$$\mathrm{k}_z^2 + \mathrm{k}_\perp^2 = \frac{c^2}{v_A^2}.$$

The radial dependence of B_z has the functional form of

$$B_z(r) = \mathrm{A}_1 J_m(k_c r) + \mathrm{A}_2 Y_m(k_c r),$$

where A_1 and A_2 are coefficients to be determined, $J_m(k_c r)$ and $Y_m(k_c r)$ are the Bessel function of the first and second kind with the order m, and $k_c^2 = k^2 - k_z^2$. The wave E_r and E_θ components can be written in terms of B_z:

$$E_\theta = \frac{i\omega\epsilon_{xy}}{\gamma^2+\epsilon_{xy}^2}\frac{im}{r}B_z + \frac{i\omega\gamma}{\gamma^2+\epsilon_{xy}^2}\frac{d}{dr}B_z\,;$$
$$E_r = \frac{i\omega\epsilon_{xy}}{\gamma^2+\epsilon_{xy}^2}\frac{d}{dr}B_z - \frac{i\omega\gamma}{\gamma^2+\epsilon_{xy}^2}\frac{im}{r}B_z,$$

where $\gamma = k_z^2 - \epsilon_{xx}$. From the boundary conditions of $E_\theta(\mathrm{a}) = E_\theta(b) = 0$, the following two equations are obtained:

$$\mathrm{A}_1 J_m'(k_c a) + \mathrm{A}_2\, Y_m'(k_c a) = 0;$$
$$\mathrm{A}_1 J_m'(k_c b) + \mathrm{A}_2\, Y_m'(k_c b) = 0.$$

Since non-trivial solutions are of interest, this set leads to the transcendental eigenvalue equation for k_c:

$$J_m'(k_c a)\, Y_m'(k_c b) = J_m'(k_c b)\, Y_m'(k_c a),$$

which can be solved for k_c numerically. As an example, Fig. 3 shows the first four E_θ profiles normalized to its maximum from the cutoff k_c values of 31.5, 40.1, 57.9, and 79.1 m^{-1} for the case of m = 30 with the two boundaries: a = 0.88 m and b = 1.01 m. The first two roots exhibit a functional form that is similar to the sine function, the standing wave pattern in the parallel plate waveguide mode, similar to the mode structure seen in Fig. 1. The subsequent roots demonstrate one full and two full cycles within the radian range, illustrating the standing wave nature in the transverse direction. Note that, for a self-consistent solution, the interface matching of the wavefields [7] or numerical modelings are needed (as shown in the next section), which will determine the details of the mode structure.

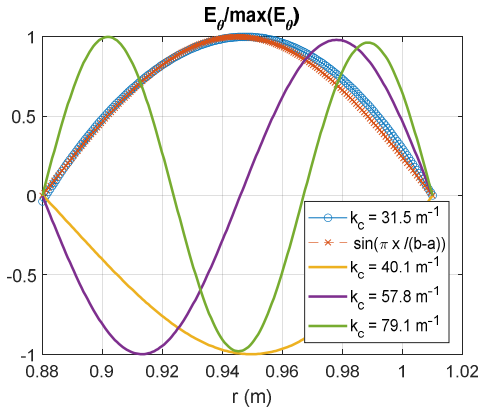

Fig. 3. The $\boldsymbol{E_\theta}$ profile normalized to its maximum, using the k_c roots found from the transcendental equation: $\boldsymbol{J_m'(k_c a)\, Y_m'(k_c b) = J_m'(k_c b)\, Y_m'(k_c a)}$ for m = 30 with the two boundaries: a = 0.88 m and b = 1.01 m. The first two roots exhibit a functional form that is similar to the sine function, the standing wave pattern in the parallel plate waveguide mode.

4 Petra-M 2D cylinder model

Fig. 4 illustrates the 2D cylinder model implemented in the Petra-M finite element multi-physics platform [11]. The annulus SOL density is constant at $n_{SOL} = 3\text{x}10^{18}$ m^{-3} and the core density is constant at $n_{core} = 3\text{x}10^{19}$ m^{-3}. There is a density step at the interface. The two boundaries are a = 91 cm (94 cm) and b = 101 cm for an

annulus width of 10 cm (7 cm). The outer boundary condition is a perfect electric conductor. The magnetic field is axial only: B_z = 0.4 T. These dimensions are comparable to those in NSTX. To control the degree of wave collisional damping for minimizing the wave interference effect and visualizing mode coupling to the SOL annulus, the temperatures are intentionally assigned to low values of T_{core} = 50 eV and T_{SOL} = 5 eV in the core and SOL regions, respectively. The wave frequency is 30 MHz. A constant antenna current density of 1 A/m² is applied along the outer arc length (central angle of 72°) at two different wave parallel wavenumbers, $k_{||}$ = 5 m^{-1} and 12 m^{-1}. As shown in Fig. 5, the half-wavelength condition in the annulus SOL can be evaluated from the HHFW dispersion. For the input wave parallel phasing of $k_{||}$ = 5 m^{-1} (12 m^{-1}), the radial gap width greater than the critical width of $\Delta_{crit} = \lambda_{\perp}/2$ = 8.1 cm (17.8 cm) can support the waveguide mode. Note that, for the description of the scattering of an RF plane wave by a cylindrical plasma filament, a full-wave analytic model was developed in the past using a 2D cylinder geometry [12].

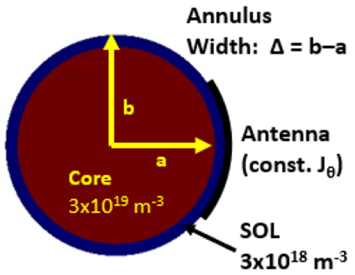

Fig. 4. Geometry of the 2D cylinder model in Petra-M. The annulus gap width is $\Delta = b - a$. The background axial B-field is B_0 = 0.4 T. The antenna current density with a finite azimuthal extent is applied to the plasma medium.

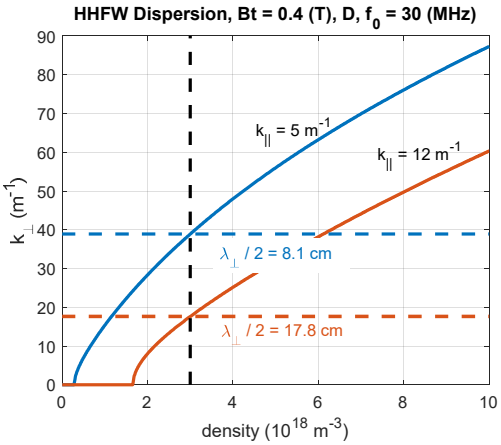

Fig. 5. HHFW dispersion at two wave parallel numbers: $k_{||}$ = 5 m^{-1} (blue) and 12 m^{-1} (red). Two horizontal dashed lines indicate the corresponding perpendicular wavenumbers at the annulus SOL density of n_{SOL} = 3x10^{18} m^{-3} (black vertical dashed line) in Fig. 4.

Figs. 6 and 7 compare the axial wave magnetic field (B_z) distribution below and above the critical gap width (Δ = 8.1 cm) for the wave parallel wavenumber $k_{||}$ = 5 m^{-1}. As shown in Fig. 6, no propagating waveguide mode is visible in the SOL with a gap width of Δ = 7 cm, which is below the critical gap width. The wavefield exhibits core propagation, whose power is dissipated by the artificial electron-ion collisions in the simulation. This is similar to a typical ICRF coupling and propagation pattern.

In contrast, Fig. 7 shows the waveguide mode supported in the annulus SOL with a gap width of 10 cm, which can be distinguished from the wavefield in the core region. The collisional damping (T_{SOL} = 5 eV) introduces power dissipation, resulting in the dissipation of the mode structure in the annular SOL as it propagates away from the antenna (exciter) azimuthally.

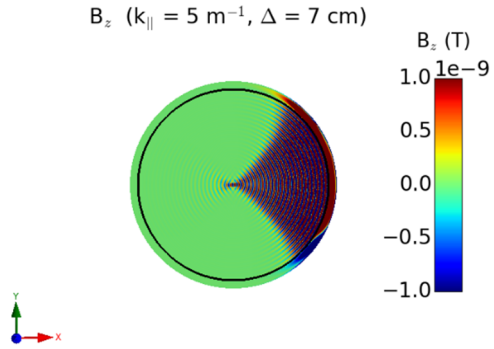

Fig. 6. Axial wave magnetic field (B_z) distribution for the wave phasing $k_{||}$ = 5 m^{-1}. The annulus SOL gap width is Δ = 7 cm, which is below the critical width (see Fig. 5). B_0 = 0.4 T. The black contour indicates the core-SOL interface. a = 0.94 m and b = 1.01 m.

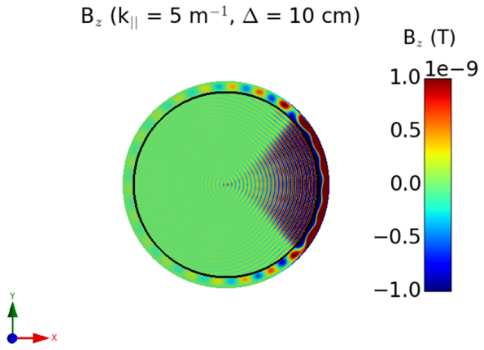

Fig. 7. Axial wave magnetic field (B_z) distribution for the wave phasing $k_{||}$ = 5 m^{-1}. The annulus SOL gap width is Δ = 10 cm, above the critical width (see Fig. 5). The waveguide mode in the annulus SOL is supported. B_0 = 0.4 T. The black contour indicates the core-SOL interface. a = 0.91 m and b = 1.01 m.

Fig. 8 compares the profiles of the collisional power density for the two cases in Fig. 6 (narrower gap) and Fig. 7 (wider gap). Here, the collisional power dissipation is used to evaluate the power coupled to the annulus SOL plasma, which is 49% of the total collisional power dissipated when the waveguide mode is supported, compared to 24% in the narrower gap case. In the latter, collisional dissipation is dominated by the

power crossing the SOL before being coupled to the core region. This example indicates that a significant fraction of power (~25%) can be coupled to the waveguide mode if the wavelength condition is met, suggesting an essential role for the outer gap. While this is a simplified and ideal condition, the waveguide mode could be formed in a similar manner in the experiment between the LCFS and the metallic wall. Note that this work has not examined the sensitivity of the power ratio to the temperatures in both regions. As long as power is fully dissipated in a single-pass sense, it is expected that the power ratio will be more sensitive to the annulus temperature than to the core temperature since the wave power needs to cross the annulus before reaching the core region.

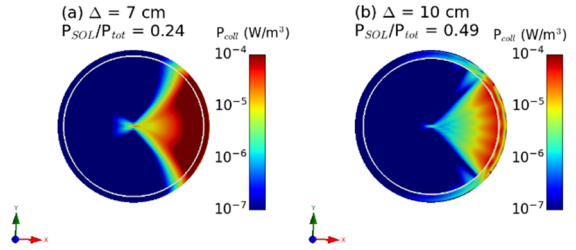

Fig. 8. Collisional power dissipation profile for the wave parallel phasing of $k_{||}$ = 5 m^{-1} with the gap width of (a) Δ = 7 cm in Fig. 6 and (b) Δ = 10 cm in Fig. 7. The white contour indicates the core-SOL interface.

axial and azimuthal components are dominant. Of the two, the axial component exhibits the highest power level. Nevertheless, its power flow is not purely axial (parallel to the magnetic field) in the annulus. Thus, this mode is NOT expected to cause a purely field-aligned wavefield structure (e.g., slow wave) in a 3D geometry.

It is worth noting that the azimuthal profile of the Ponyting flux components exhibits a coherent structure, indicating a specific azimuthal mode is being excited (see also the wave magnetic field in Fig. 7). The ongoing analysis indicates that such an azimuthal mode arises from the annulus resonance mode, which possesses a high azimuthal mode number. On the other hand, the wave components in the core region are dominated by low azimuthal mode numbers. The antenna spectrum in the azimuthal mode space [7] is thought to be critical in determining the annulus resonance, which will be reported in future work.

Figs. 10 and 11 show the cases where the annulus waveguide mode can be suppressed at a fixed gap width Δ = 10 cm by varying the input phasing or the background magnetic field. First, Fig. 10 demonstrates that a higher parallel wavenumber ($k_{||}$ = 12 m^{-1}) suppresses the waveguide mode due to a longer perpendicular wavelength compared to the $k_{||}$ = 5 m^{-1} case (Fig. 7). The dispersion curve in Fig. 5 indicates that the half-wavelength condition for the given annulus

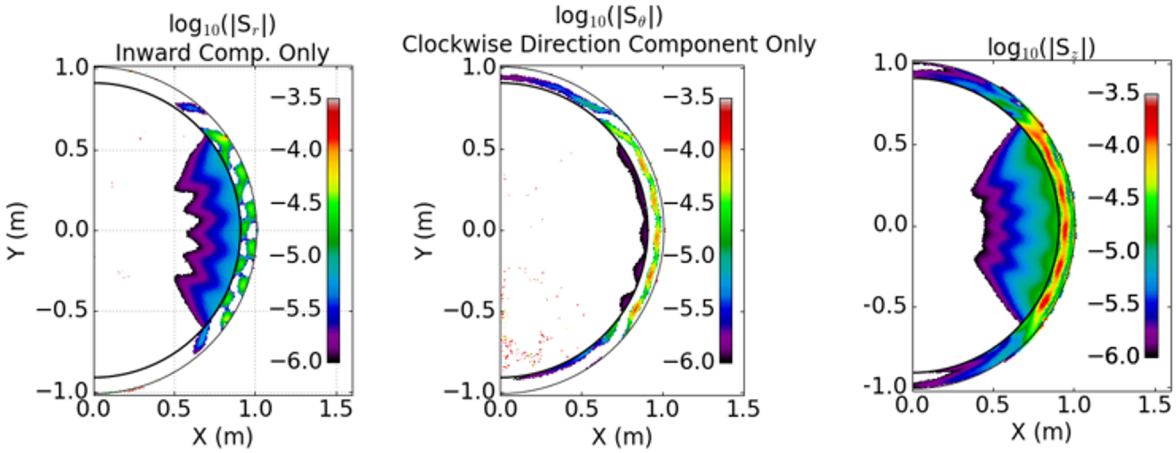

Fig. 9. Ponyting fluxes in a logarithmic scale: (left) radial, (middle) azimuthal, and (right) axial components for the wave phasing $k_{||}$ = 5 m^{-1} with Δ = 10 cm and B_0 = 0.4 T.

Fig. 9 compares the radial, azimuthal, and axial Ponyting flux components in a logarithmic scale for the input phasing of $k_{||}$ = 5 m^{-1} and a width of 10 cm. For the radial (azimuthal) components, only the inward (clockwise direction) components are plotted to visualize the relative magnitudes among the flux components, causing the blank regions in the figures. Also, the colorbar represents the logarithm of the absolute magnitude of each component to highlight the magnitude variation. In the core region, the radial and axial components are dominant, which is a characteristic of the fast wave. Meanwhile, in the annulus region, the

density is wider (Δ_{crit} = 17.8 cm) for $k_{||}$ = 12 m^{-1}. Second, increasing the background magnetic field has a similar effect, as shown in Fig. 11. It displays the wavefield for a fixed $k_{||}$ = 5 m^{-1} when B_0 is increased from 0.4 T to 0.8 T (to be expected on NSTX-U). At this higher field strength, the HHFWs still possess a propagating $k_{\perp}$, while the perpendicular wavelength is increased. The critical width increases to $\Delta_{crit} = \lambda_{\perp}/2$ = 16.7 cm. Note that the ICRF fast wave dispersion $\omega \approx k_{\perp} V_A \sqrt{1 + c^2 k_{||}^2 / \omega_{pi}^2}$ is a still good approximation for HHFW above the fast wave cutoff.

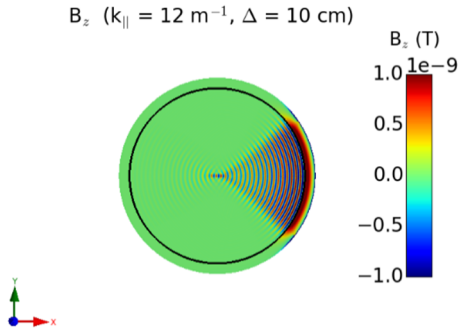

Fig. 10. Axial wave magnetic field (B_z) distribution for the wave phasing $k_{||}$ = 12 m^{-1}. The annulus SOL gap width is Δ = 10 cm, below the critical width (see Fig. 5). B_0 = 0.4 T.

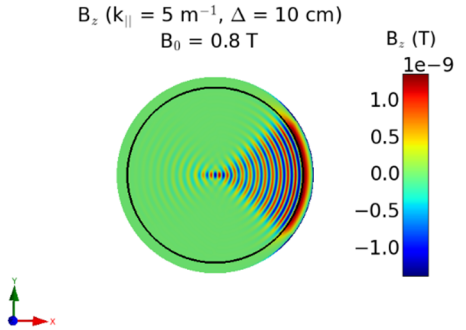

Fig. 11. Axial wave magnetic field (B_z) distribution for the wave phasing $k_{||}$ = 5 m^{-1}, but with B_0 = 0.8 T.

5. Discussion and Summary

The waveguide mode discussed here likely corresponds to surface waves or cavity modes observed in previous 2D/3D HHFW modeling. In those simulations, the large domain size beyond the LCFS may have masked the onset condition of this mode, particularly at a lower parallel phasing, since its minimum width required is narrower. As the SOL density is increased, the fast wave cutoff condition is relaxed within the simulation domain, allowing this mode to be inherently supported. It should be noted that past studies have noted such a geometric dependency. In one study [4], the radial wavenumber of the SOL mode was represented by $k_r = \pi/L$ where L is the radial width between the R-cutoff and the outer simulation boundary. Another study [5] reported that reducing the physical distance between the LCFS and the wall boundary limits the poloidal extent of HHFW propagation, even though the fast wave cutoff remains open. The waveguide mode discussed here is likely to have played a role.

As noted in the introduction section, one critical aspect of the waveguide mode that needs to be answered is the excitation mechanism. The guiding mechanism is only discussed here. From the initial results (e.g., Figs. 7 and 9), the modes with a high azimuthal mode number are thought to be excited as a result of annulus resonance, and this is being investigated.

In a related manner, recent HHFW modeling using a NSTX-U vessel geometry with a divertor SOL density profile from a finite-element two-point model exhibits a clear dependence of mode onset on the SOL density gradient [13]. The larger the e-folding length of the SOL density profile, the weaker the parasitic wave coupling to the SOL. The broadened density profile effectively reduces the gap width. A corresponding increase in coupling of the wavefield to the core plasma is numerically observed, which recovers the conventional ICRF coupling picture, thus bridging our understanding of coupling physics. Note that, due to its longer wavelength, the ICRF regime can exhibit cavity resonance in a global sense [14] between the antenna and the ion-ion hybrid layer at the plasma core, accompanied by an increase in coupling resistance.

Power dissipation mechanisms remain unresolved. Collisions involving electron-ion/neutral interactions could be important. Mode conversion to slow waves, assisted by filamentary turbulence in the SOL, has also been identified [15], which could be responsible for the field-aligned RF-enhanced divertor heat flux pattern (RF spiral) on NSTX [16, 17] via RF sheath rectification. As shown in Fig. 9, the waveguide mode discussed here does not appear to be a purely field-aligned structure. But, the fast wave field enhancement to the SOL through this geometric waveguide mode could intensify such a mode conversion process, as both have the same dependence on $k_{||}$, density, and B-field.

In the upcoming experiments on NSTX-U, successful core coupling of HHFW power, particularly at low parallel phasing, is desired for efficient current drive for non-inductive scenario development. The 1 T operation with up to 2 MA will enable control of the edge/SOL in terms of the Greenwald fraction, along with wall conditioning and position scans, to examine the role of the outer gap. So far, it has been suggested that controlling the density in front of the antenna below the R-cutoff can prevent the onset of fast wave propagation. Meanwhile, the work here suggests an alternative approach when the SOL density exceeds the cutoff density by narrowing the gap width to the extent that the half-wavelength condition is *not* supported. However, experimental constraints may prevent reducing the outer gap to the required level, particularly due to neutral beam ion interactions with the HHFW antenna. Previously, an outer gap of 7 to 8 cm was required [18]. Density profile broadening can be another alternative approach; however, profile tailoring may still pose a challenge. In this sense, the 1T operation is expected to help from the following two perspectives. First, it will increase the cut-off density requirement, prohibiting fast wave coupling [1]. Second, the high field lengthens the HHFW perpendicular wavelength, which helps prevent waveguide coupling for the fixed SOL width. The low phasing gives the strictest condition for the SOL gap coupling. Higher parallel phasing will be effectively coupled to the core for accessing the electron heating regime.

Looking beyond HHFW operation on NSTX-U, geometric considerations may be critical, particularly for reactor-relevant ICRF/HHFW actuators whose placement will be far from the plasma. For example, the

low-field (B_0 = 2.65 T) D(H) operation on ITER [19] will result in a shorter wavelength than that in the standard field (5.3 T). A nominal distance from the LCFS and the antenna is ~20 cm on ITER, and the geometric condition may be satisfied if the phasing is low enough and the SOL density remains high enough across the SOL (e.g., $\lambda_\perp/2 \approx 20$ cm for $k_\perp \approx 15.7$ m^{-1} with $k_{||} = 4$ m^{-1} at $n_e = 5\text{x}10^{18}$ m^{-3} and $B_{SOL} = 2$ T). At the same time, the impact of the density gradient will also need to be assessed, which can help suppress the mode onset.

In summary, this paper discussed the propagation of HHFWs in the SOL of the NSTX-U spherical tokamak from the viewpoint of the waveguide mode. The analytical and computational models suggest that the fast wave can couple to the bounded region in the SOL between the steep density region and the outer wall. The half-wavelength radial width is critical, and the waveguide mode is sensitive to the relative size of the wavelength to the SOL gap width. Controlling edge/SOL conditions will be essential to prevent parasitic coupling, which has implications for reactor-relevant ICRF actuators placed far from the plasma. The upcoming NSTX-U experiments will serve as an important testbed for testing the latest understanding.

This work was supported by the U.S. DoE awards, DE-SC0021120, DE-AC02-09CH11466, and DE-AC02-05CH11231 using NERSC award FES-ERCAP0027700.

References

1. J. C. Hosea et al., High harmonic fast wave heating efficiency enhancement and current drive at longer wavelength on the National Spherical Torus Experiment, Phys. Plasmas **15,** 056104 (2008). https://doi.org/10.1063/1.2837051
2. S. H. Stix, Waves in Plasmas (American Institute of Physics, 1992)
3. D. L. Green et al., Predicting high harmonic ion cyclotron heating efficiency in tokamak plasmas, Phys. Rev. Lett. **107**, 145001 (2011). https://doi.org/10.1103/PhysRevLett.107.145001
4. N. Bertelli et al., Full wave simulations of fast wave heating losses in the scrape-off layer of NSTX and NSTX-U, Nucl. Fusion **54**, 083004 (2014). https://doi.org/10.1088/0029-5515/54/8/083004
5. E. H. Kim et al., Effect of wall boundary on the scrape-off layer losses of high harmonic fast wave in NSTX and NSTX-U, Phys. Plasmas **26**, 062501 (2019). https://doi.org/10.1063/1.5091579
6. N. Bertelli et al., 3D full wave fast wave modeling with realistic HHFW antenna geometry and SOL plasma in NSTX-U, Nucl. Fusion **62**, 126046 (2022), https://doi.org/10.1088/1741-4326/ac9690
7. R. Perkins et al., Resonance in fast-wave amplitude in the periphery of cylindrical plasmas and application to edge losses of wave heating power in tokamaks, Phys. Plasmas **23**, 070702 (2016). https://doi.org/10.1063/1.4954899
8. D. M. Pozar, Microwave Engineering (John Wiley and Sons, 2012)
9. N. Bertelli et al., Full wave simulations of fast wave efficiency and power losses in the scrape-off layer of tokamak plasmas in mid/high harmonic and minority heating regimes, Nucl. Fusion **56,** 016019 (2015). https://doi.org/10.1088/0029-5515/56/1/016019
10. D. G. Swanson, Plasma Waves (Institute of Physics, 2003)
11. S. Shiraiwa et al., RF wave simulation for cold edge plasmas using the MFEM library, EPJ Web Conf. **157,** 03048 (2017). https://doi.org/10.1051/epjconf/201715703048
12. A. Ram and K. Hizanidis. Scattering of radio frequency waves by cylindrical density filaments in tokamak plasmas, Phys. Plasmas **23**, 022504 (2016). https://doi.org/10.1063/1.4941588
13. R. De Levante Rodriguez, Study of high harmonic fast waves interactions in the scrape off layer of NSTX-U, Master Thesis, MIT (2025).
14. Y. Ogawa et al., Analysis of the loading resistance for ICRF heating experiments in ASDEX, Plasma Phys. Contr. Fus. **33**, 155 (1991). https://doi.org/10.1088/0741-3335/33/2/005
15. W. Tierens et al., On the origin of high harmonic fast wave edge losses in NSTX, Nucl. Fusion **62**, 096011 (2022). https://doi.org/10.1088/1741-4326/ac7c7d
16. R. J. Perkins et al., High-harmonic fast-wave power flow along magnetic field lines in the scrape-off layer of NSTX, Phys. Rev. Lett. **109**, 045001 (2012). https://doi.org/10.1103/PhysRevLett.109.045001
17. R. J. Perkins et al., The role of rectified currents in far-field RF sheaths and in SOL losses of HHFW power on NSTX, Nucl. Mater. Energy **12**, 283 (2017). https://doi.org/10.1016/j.nme.2017.04.013
18. J. C. Hosea, HHFW Operations on NSTX-U, Physics Operations Course, PPPL (2015). https://nstx.pppl.gov/DragNDrop/Operations/Physics_Operations_Course/15%20Hosea_HHFW%20operations_fin-2.pdf
19. W. Helou, The ITER ICRF system under the new ITER baseline: latest updates and technological development, 25th Topical Conference on Radio-Frequency Power in Plasmas, Schloss Hohenkammer, Germany, May 19-22 (2025), https://www.ipp.mpg.de/5487515/Talks